

The elderly among the oldest: new evidence for extremely metal-poor RR Lyrae stars[★]

V. D’Orazi^{1,2}, V. Braga³, G. Bono^{1,3}, M. Fabrizio³, G. Fiorentino³, N. Storm⁴, A. Pietrinferni⁵, C. Sneden⁶, M. Sánchez-Benavente^{7,8}, M. Monelli^{7,8,3}, F. Sestito⁹, H. Jönsson¹⁰, S. Buder^{11,12}, A. Bobrick¹³, G. Iorio¹⁴, N. Matsunaga^{15,16}, M. Marconi¹⁷, M. Marengo¹⁸, C. E. Martínez-Vázquez¹⁹, J. Mullen²⁰, M. Takayama²¹, V. Testa³, F. Cusano²², and J. Crestani^{1,3}

¹ Department of Physics, University of Rome Tor Vergata, via della ricerca scientifica 1, 00133, Rome, Italy
e-mail: vdorazi@roma2.infn.it

² INAF – Osservatorio Astronomico di Padova, vicolo dell’Osservatorio 5, 35122, Padova, Italy

³ INAF – Osservatorio Astronomico di Roma, via Frascati 33, Monte porzio catone, Italy

⁴ Max Planck Institute for Astronomy, Königstuhl 17, 69117 Heidelberg, Germany

⁵ INAF – Osservatorio Astronomico d’Abruzzo, via Maggini sn, I-64100 Teramo, Italy

⁶ Department of Astronomy and McDonald Observatory, The University of Texas, Austin, TX 78712, USA

⁷ IAC - Instituto de Astrofísica de Canaria, calle Via Lactea s/n, E-38205 La Laguna, Tenerife, Spain

⁸ Departamento de Astrofísica, Universidad de La Laguna, E-38206 La Laguna, Tenerife, Spain

⁹ Centre for Astrophysics Research, Department of Physics, Astronomy and Mathematics, University of Hertfordshire, Hatfield, AL10 9AB, UK.

¹⁰ Materials Science and Applied Mathematics, Malmö University, SE-205 06 Malmö, Sweden

¹¹ Research School of Astronomy & Astrophysics, Australian National University, ACT 2611, Australia

¹² Center of Excellence for Astrophysics in Three Dimensions (ASTRO-3D), Australia

¹³ Physics Department, Technion –Israel Institute of Technology, Haifa 32000, Israel

¹⁴ Departament de Física Quàntica i Astrofísica, Institut de Ciències del Cosmos, Universitat de Barcelona, Martí i Franqués 1, 08028 Barcelona, Spain

¹⁵ Department of Astronomy, School of Science, The University of Tokyo, 7-3-1 Hongo, Bunkyo-ku, Tokyo 113-0033, Japan

¹⁶ Laboratory of Infrared High-resolution spectroscopy (LiH), Koyama Astronomical Observatory, Kyoto Sangyo University, Motoyama, Kamigamo, Kita-ku, Kyoto 603-8555, Japan

¹⁷ INAF – Osservatorio Astronomico di Capodimonte, salita Moiariello 16, I-80131 Napoli, Italy

¹⁸ Department of Physics, Florida State University, 77 Chieftain Way, Tallahassee, FL32306, USA

¹⁹ International Gemini Observatory/NSF NOIRLab, 670 N. A’ohoku Place, Hilo, Hawai’i, 96720, USA

²⁰ Department of Physics and Astronomy, Vanderbilt University, Nashville, TN 37240, USA

²¹ Nishi-Harima Astronomical Observatory, Center for Astronomy, University of Hyogo, 407-2, Nishigaichi, Sayo-cho, Hyogo 679-5313, Japan

²² INAF – Osservatorio Astrofisica e Scienza dello Spazio, via Gobetti 93/3, Bologna, Italy

Received: 28 November 2024 | Accepted 6 January 2025

ABSTRACT

We performed a detailed spectroscopic analysis of three extremely metal-poor RR Lyrae stars, exploring uncharted territories at these low metallicities for this class of stars. Using high-resolution spectra acquired with HARPS-N at TNG, UVES at VLT, and PEPSI at LBT, and employing Non-Local Thermodynamic Equilibrium (NLTE) spectral synthesis calculations, we provide abundance measurements for Fe, Al, Mg, Ca, Ti, Mn, and Sr. Our findings indicate that the stars have metallicities of $[\text{Fe}/\text{H}] = -3.40 \pm 0.05$, -3.28 ± 0.02 , and -2.77 ± 0.05 for HD 331986, DO Hya, and BPS CS 30317-056, respectively. Additionally, we derived their kinematic and dynamical properties to gain insights into their origins. Interestingly, the kinematics of one star (HD 331986) is consistent with the Galactic disc, while the others exhibit Galactic halo kinematics, albeit with distinct chemical signatures. We compared the $[\text{Al}/\text{Fe}]$ and $[\text{Mg}/\text{Mn}]$ ratios of the current targets with recent literature estimates to determine whether these stars were either accreted or formed in situ, finding that the adopted chemical diagnostics are ineffective at low metallicities ($[\text{Fe}/\text{H}] \lesssim -1.5$). Finally, the established horizontal branch evolutionary models, indicating that these stars arrive at hotter temperatures on the Zero-Age Horizontal Branch (ZAHB) and then transition into RR Lyrae stars as they evolve, fully support the existence of such low-metallicity RR Lyrae stars. As a consequence, we can anticipate detecting more of them when larger samples of spectra become available from upcoming extensive observational campaigns.

Key words. Stars: abundances – Stars: Population II – Stars: variables: RR Lyrae – Galaxy: abundances

[★] Based on observations acquired at the Telescopio Nazionale Galileo under program A43DDT3, on a DDT program with PEPSI at LBT

(2021-2022, PI Crestani) and on VLT ESO programs 69.C-0423(A) and 165.N-0276(A).

1. Introduction

Since the publication of the seminal paper by Baade (1958), RR Lyrae stars (RRLs) have become reliable indicators of ancient stellar populations (Layden et al. 1996; Sneden et al. 2017; Preston et al. 2019; Braga et al. 2021, and references therein). These stars are radial variables that pulsate in various modes: the fundamental mode (RRab), the first overtone mode (RRc), and both the fundamental and first overtone modes simultaneously (RRd). Their periods typically range from a few hours to just under a day. RRLs are low-mass horizontal-branch (HB) stars, with masses between ≈ 0.50 and $0.85 M_{\odot}$ (Marconi et al. 2015; Marsakov et al. 2019; Bobrick et al. 2024), which burn helium in their cores and hydrogen in a surrounding shell. Compared to similar stellar tracers, RRLs offer three key advantages. *i)* They are ubiquitous, meaning they have been identified in all stellar systems hosting old stellar populations. *ii)* They are accurate primary distance indicators and obey the well-defined Period-Luminosity (PL) relation for wavelengths longer than the *R*-band. *iii)* They can be easily identified due to the distinctive coupling between the shape of their light curves and the pulsation period. There are some classification difficulties for RRc variables that overlap with geometrical (binaries) and Delta Scuti variables. Still, pulsation observable (the ratio of luminosity amplitudes) can be adopted to improve their identification (Mullen et al. 2022). The main drawback is that they are several magnitudes fainter than Miras, Classical Cepheids, and type II Cepheids.

Baade was the first to observe differences in the light curves of RRLs between those located in the bulge and those in globular clusters and the halo. Even before obtaining spectroscopic measurements, he proposed that RRLs in the bulge were more metal-rich. This hypothesis was later confirmed by the pioneering spectroscopic studies conducted by Preston (1959, 1964), which demonstrated that many field RRLs were indeed metal-rich and exhibited disc kinematics. The kinematics were more typical of thick disc stars and it took over thirty years until another critical spectroscopic investigation by Layden (1995) identified, through the ΔS method¹, metal-rich RRLs with thin disc kinematics. A few years earlier, Walker & Terndrup (1991) utilised the ΔS method to provide the first evidence of bulge RRLs approaching solar iron abundance. Subsequently, Wallerstein et al. (2011) employed the Ca II triplet and confirmed the existence of solar-metallicity RRLs.

Recent spectroscopic studies have shown that RRLs exhibit α -enhanced abundance patterns in metal-poor stars ($[\text{Fe}/\text{H}] \leq -1$) and display a composition closer to the solar mixture in more metal-rich stars (For et al. 2011; Chadid et al. 2017; Sneden et al. 2017; Magurno et al. 2018). A similar conclusion was also reached by Marsakov et al. (2019, and references therein). Recent studies by Crestani et al. (2021b,a); D’Orazi et al. (2024) have contributed to this field by providing accurate abundances for several α elements, such as magnesium, calcium, and titanium. Using relatively large(*r*) samples, these investigations revealed that RRLs with iron abundances close to solar levels display sub-solar α -element abundances.

The results from these studies indicate that RRLs span over 2.5 dex in iron abundance and exhibit a wide range in α -element abundances. In this context, the low-end metallicity distribution is mainly represented by RRLs in Galactic globular clusters, particularly those in M68, M92, and M15, with iron abundances

around -2.5 dex. Unexpected discoveries of extremely metal-poor (EMP, $[\text{Fe}/\text{H}] \lesssim -2.7$) RRLs were made by Hansen et al. (2011), who identified two field RRLs with iron abundances of ≈ -2.8 , and by Crestani et al. (2021a), who determined that DO Hya also shares a similar iron abundance. Surprisingly, Matsunaga et al. (2022) discovered a field RRL with disc kinematics and an iron abundance possibly even more metal-poor than $[\text{Fe}/\text{H}] \approx -3$. The lack of high-resolution optical spectra initially limited abundance analyses of these stars. This study aims to explore the lower limits of metallicity for field RRLs, a poorly explored region compared to our understanding of RR Lyrae in clusters. We determine detailed elemental abundances for these stars and, through dynamical and chemical analyses, investigate their origin and association with specific Galactic populations. This paper presents the first detailed spectroscopic analysis of EMP field RRLs, which exist in a metallicity range even lower than that typically found in globular clusters.

2. Spectroscopic analysis

Our observational efforts focused on the three currently known EMP RRLs field stars: HD 331986, DO Hya, and BPS CS 30317-056. We employed the HARPS-N at the Telescopio Nazionale Galileo (TNG, Roque de los Muchachos, Spain) spectroscopic data of HD 331986 (also known as Matsunaga’s star; Matsunaga et al. 2022) that exhibit a nominal resolution of $R=115,000$ (Cosentino et al. 2014). This analysis focused on observations conducted near the pulsation phase $\phi = 0.87$, which occurs at the onset of rising light². At this stage, effective temperatures are still close to their minimum values within the pulsation cycle (Magurno et al. 2019), enabling us to enhance the detectability of spectral features. The selected spectrum, recorded on 24 July 2021, offers a spectral range from 3900 to 6900 Å and a signal-to-noise ratio (SNR) of 36 per pixel around 6000 Å. The T_{eff} was determined using a Non-Local Thermodynamic Equilibrium (NLTE) approach for H_{α} line fitting, and the surface gravity was inferred through the ionisation equilibrium of iron absorption lines. Our analysis used the Python wrapper for TurboSpectrum 2020, TSPy (Gerber et al. 2023; Storm & Bergemann 2023), which enables the calculation of NLTE synthetic spectra in real-time and accounts for best-fit determinations against observed spectra using the Nelder-Mead algorithm (e.g. Storm & Bergemann 2023). The microturbulent velocity (V_{mic}) was determined by removing any evident trends between the Reduced Equivalent Width (REW) and the NLTE iron abundances derived from Fe I lines. All parameters and abundances reported in this study are based on NLTE calculations; our recent publication (D’Orazi et al. 2024) provides a comprehensive discussion of these methodologies and their implications. For completeness, we also reviewed additional spectra obtained with HARPS-N (three spectra at hotter phases of $\phi=0.07, 0.431, 0.636$) and PEPSI at the Large Binocular Telescope (Strassmeier et al. 2015), which consistently corroborated our metallicity estimates within an uncertainty margin of 0.1 dex.

To mitigate systematic errors and standardise the metallicity scale for the two most metal-deficient RRLs ever reported, we re-evaluated the spectrum of DO Hya, initially included by Crestani et al. (2021b); observational details regarding this spectrum are provided in the referenced study. Our elemental analysis extended beyond iron, encompassing determinations of abun-

¹ This method exploits the strengths of Ca II H,K and hydrogen Balmer lines to estimate the metallicity (see e.g. Crestani et al. 2021a, and references therein).

² Note that we adopted, as reference epoch, the time of the mean magnitude on the rising branch and not the typical time of maximum light (Inno et al. 2015; Braga et al. 2021)

dances for aluminium (Al), magnesium (Mg), calcium (Ca), titanium (Ti), manganese (Mn), and strontium (Sr), with NLTE spectral fitting for all the species under scrutiny (see details provided in Table A.1). An example of the spectral synthesis technique for the Al I line at 3944 Å and the Sr II line at 4077 Å is shown in Figure 1. Unfortunately, we were unable to determine the carbon abundances for our sample stars. Nevertheless, our spectral analysis suggests that substantial enhancements in the [C/Fe] ratios (like those inferred in Carbon-Enhanced Metal-Poor stars -CEMP) are unlikely, as we establish upper limits of $[C/Fe] \lesssim 1$. For completeness, we report that Matsunaga et al. (2022) established an upper limit of $[C/H] \leq -2.5$, which aligns well with our estimate when using our metallicity value of $[Fe/H] = -3.40$. It is worth recalling that in their study they could only determine an upper limit on iron abundance of $[Fe/H] \leq -2.5$. These findings indicate a distinct behaviour of our three EMP RRLs compared to the CEMP RRLs identified by Kennedy et al. (2014). Notably, they inferred $[C/Fe] = +1.35$ for WY Vir, which has a metallicity of $[Fe/H] = -2.65$.

In the Introduction, we referred to the work by Hansen et al. (2011), who identified two exceptionally metal-poor RRLs: BPS CS 30317-056 and BPS CS 22881-039. The re-evaluation focused on BPS CS 30317-056 and is discussed further in the subsequent sections. Our findings align with those initially reported, considering observational uncertainties. Conversely, we excluded BPS CS-22881-039 from our analysis due to its significantly broad spectral features. This broadening, likely due to high macroturbulence velocity, introduces large uncertainties in metallicity measurements, potentially exceeding 0.3 dex. This assessment aligns with findings from Crestani et al. (2021b), who, through analysis of two spectra at different phases, reported metallicity values of $[Fe/H] = -2.33$ and $[Fe/H] = -2.66$. In adherence to a conservative approach that prioritises the inclusion of only robust abundance data, we decided to omit BPS CS-22881-039 from our discussion.

3. Results and discussion

This paper presents the first comprehensive chemical and dynamical analysis of the three most metal-poor RRLs ever detected. Our study examines the stars’ origin (as detailed in the following Section 3.1) and compares observational data with theoretical evolutionary models to better understand their fundamental properties (see Section 3.2).

3.1. Chemodynamics of our EMP RR Lyrae stars

We have determined orbital parameters using the galpy code (Bovy 2015), adopting the McMillan (2017) Galactic potential. For these calculations, we adopted the Sun’s Galactocentric location as $R_{\odot} = 8.122$ kpc (GRAVITY Collaboration et al. 2018) and $z_{\odot} = 20.8$ pc (Bennett & Bovy 2019), while as 3D components of the Sun’s velocity, we used $(U_{\odot}, V_{\odot}, W_{\odot}) = (12.9, 245.6, 7.78)$ km s⁻¹ (Drimmel & Poggio 2018). The circularity of the orbits λ_z (see e.g. Massari et al. 2019), defined as the angular momentum along the z -axis (J_z) normalised by the angular momentum of a circular orbit with the same binding energy (E), was used to identify the characteristics of the orbits (for details see D’Orazi et al. 2024). Based on this classification, we found that one of the stars, HD 331986, is a disc star exhibiting kinematic properties indicative of a transition between the thin and thick disc stellar populations (see also Matsunaga et al. 2022). In contrast, the other two stars display dynamical

properties characteristic of the halo (see Fig. D.1). Atmospheric parameters and abundances are listed in Table A.1. Note that v_{γ} radial velocities are based on Gaia measurements. The v_{γ} for HD331986 is based on the fit of the radial velocity time series, while for the other two RRLs, it is the simple average of the radial velocity measurements (Clementini et al. 2023).

The EMP RRLs display a consistent pattern in their α -element abundances, with Mg, Ca, and Ti levels elevated to those characteristic of older stellar populations in our Galaxy. Notably, the [Ca/Fe] ratios are somewhat lower than the Mg and Ti values. This discrepancy arises because the only available Ca I line in our spectra is the 4226 Å line, which is known to provide significantly underestimated Ca abundances in giants with equivalent widths (EW) greater than 60 mÅ. This was initially highlighted by Mashonkina et al. (2007) and Spite et al. (2012) and was extensively discussed by Sitnova et al. (2019). The [Al/Fe] ratio is widely recognised as one of the most reliable indicators for distinguishing between accreted and in-situ components of our Galaxy (see e.g. Hawkins et al. 2015, Das et al. 2020, Horta et al. 2021, 2023). In our analysis, we found that the two metal-poor, halo-like RRLs exhibit [Al/Fe] ratios that are only slightly below the solar values. Notably, the presence of the Al I line at 3944 Å is detected in both stars, as shown in the middle and bottom panel in Figure 1 for DO Hya and BPS CS 30317-056, respectively. This finding contrasts sharply with the star HD 331986, for which we could only establish a conservative upper limit of $[Al/Fe] < 0$ (upper panel of Figure 1). To get further insights on the nature of our three EMP RRLs we compare our abundances for [Mg/Mn] vs [Al/Fe], as done in the literature for the identification of special structures in the Galactic disc, such as the ancient proto-building block *Loki* by Sestito et al. (2024) or Icarus (Re Fiorentin et al. 2024). We also refer the reader to recent works by for example Bellazzini et al. (2024), Sestito et al. (2024), Nepal et al. (2024), and Zhang et al. (2024, and references therein).

Our analysis is based on optical spectroscopy with real-time NLTE spectral synthesis calculations. Therefore, a suitable choice of large-scale comparison sample would be the similarly observed/analysed GALAH survey (De Silva et al. 2015), Data Release 4 (DR4, Buder et al. 2024).

We selected giant stars with the following quality flags:

- `snr_px_ccd3` > 70 (SNR per pixel at 6500 Å > 70)
- `flag_sp` = 0 (reliable spectroscopic analysis)
- `flag_x_fe` = 0 for Fe, Mg, Mn, and Al (reliable abundances)
- $3500 \text{ K} < T_{\text{eff}} < 5500 \text{ K}$
- $\log g < 3.6$

In the left-hand panel of Figure 2, we display the relative abundances of [Mg/Mn] vs [Al/Fe] for all the selected stars from GALAH DR4, irrespective of their iron content ($[Fe/H]$), alongside our sample of EMP RRLs and the *Loki* stars introduced by Sestito et al. (2024). These *Loki* stars have not been adjusted to match the APOGEE scale, as done in the original paper. We have included dividing lines that help classify stars as either in situ or accreted, based on their [Al/Fe] and [Mg/Mn] abundance ratios, as proposed by for example Sestito et al. (2024), among the others. Most stars are situated within the low- α in situ stellar population (lower right-hand quadrant). However, there are notable concentrations in high- α in situ (upper right-hand quadrant) and low- α accreted regions (lower left-hand quadrant, but see discussion in Buder et al. 2024).

When we shift our focus to the right-hand panel of Figure 2, specifically examining stars with low metallicity ($[Fe/H] \lesssim -$

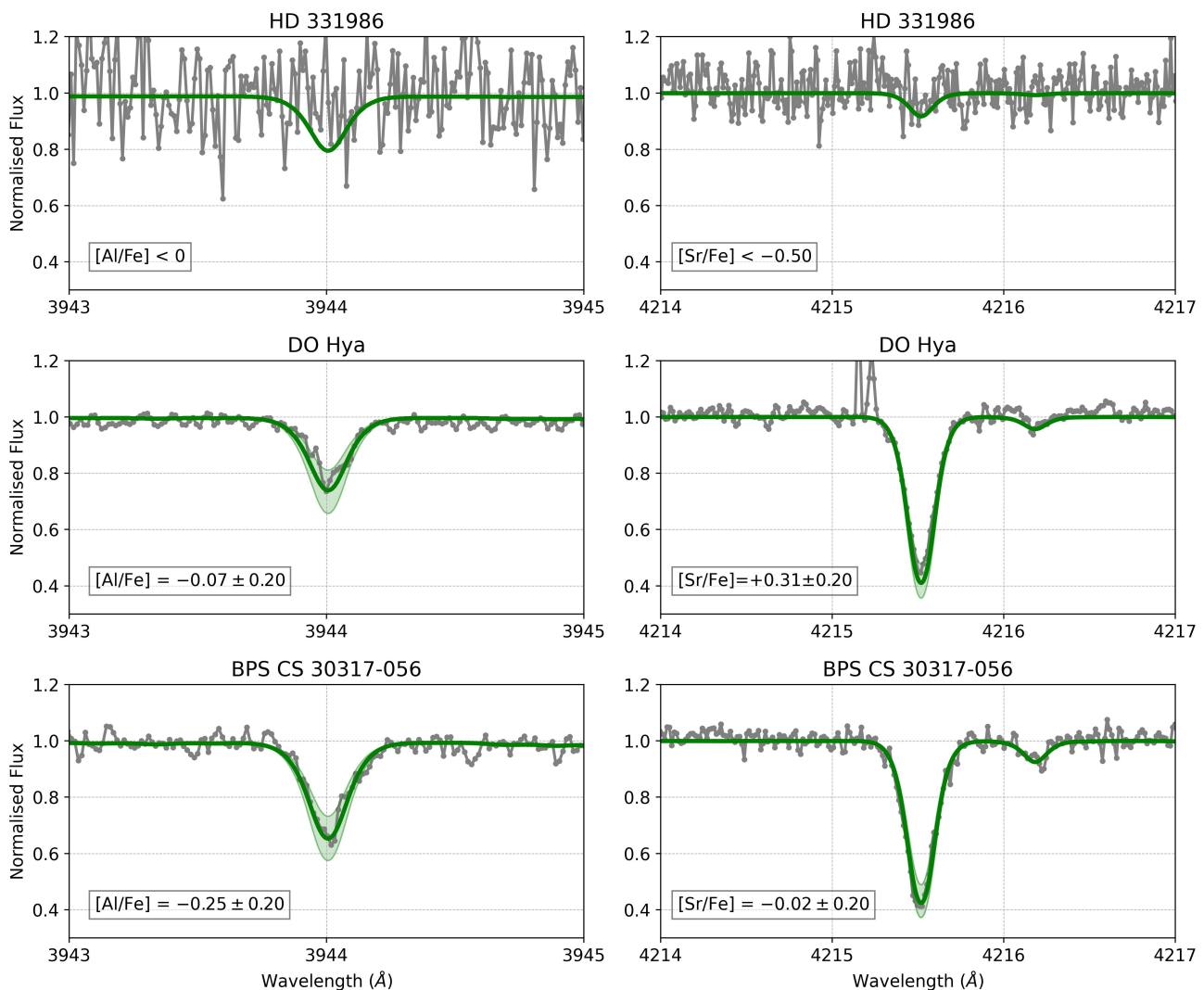


Fig. 1. Comparison of the observed (grey) and synthetic (green) spectra. For HD 331986 (upper panel), we present the upper limit synthesis, while for DO Hya (middle panel) and BPS CS 30317-056 (lower panel), we display the best-fit results along with a variation of ± 0.2 dex (shaded areas).

1.5), these stars predominantly transition to the accreted high- α region. This observation indicates that the use of aluminium-based diagnostics is quite effective at identifying stellar origins at intermediate metallicities ($[\text{Fe}/\text{H}] \gtrsim -1.5$). However, their diagnostic power seems to diminish at even lower metallicities, as also highlighted by Sestito et al. (2024). Thus, our findings suggest that chemical planes involving combinations of aluminium, magnesium, and manganese do not prove useful for distinguishing accreted structures when dealing with very low metallicities. Consequently, the origin of our observed stars remains enigmatic, as no alternative chemical abundance plane appears viable for differentiating between in situ and accreted stars at these low metallicities. This limitation presents significant challenges for employing chemical tagging techniques on very metal-poor stars, which are vital for understanding the initial phases of galaxy formation and evolution.

We were able to derive abundances for only one post-Fe peak element, strontium (Sr, $Z = 38$). In the Solar system, Sr nucleosynthesis is mainly attributed to the weak and main components of the slow (s) n -capture process (Karakas & Lattanzio 2014). However, at the metallicity of our stars, the r(apid)-process is very likely the dominant production source (see the recent re-

view by Arcones & Thielemann 2023 and references therein). HD 331986 is characterised by low $[\text{Sr}/\text{Fe}]$, in contrast to the solar abundance pattern shown by BPS CS 30317-056 and the even super-solar levels inferred in DO Hya. The evolution of n -capture elements (e.g. Sr and Ba) at low metallicity is a debated topic, especially considering the significant spread observed at metallicities $\lesssim -2.5$ dex (see the review by Cowan et al. 2021). This spread is illustrated in the lower panel of Figure 3, where our EMP RRLs are compared to the $[\text{Sr}/\text{Fe}]$ ratios as a function of metallicity for stars from Roederer et al. (2014) and François et al. (2020).

In the upper panel, we compared our upper limits on carbon abundance with literature measurements. Despite the warm temperature and low metallicity of our stars hindering a robust derivation of carbon abundances via molecular features, we can exclude the possibility that these three stars are characterised by an overabundance in $[\text{C}/\text{Fe}]$ ratios, as reported for very metal-poor carbon-enriched stars by several studies in the literature (see, e.g. Placco et al. 2014, Bonifacio et al. 2018, Arentsen et al. 2022). The three EMP RRLs align with most of the RRLs referenced by Kennedy et al. (2014), but two of their seven RRLs show a carbon overabundance.

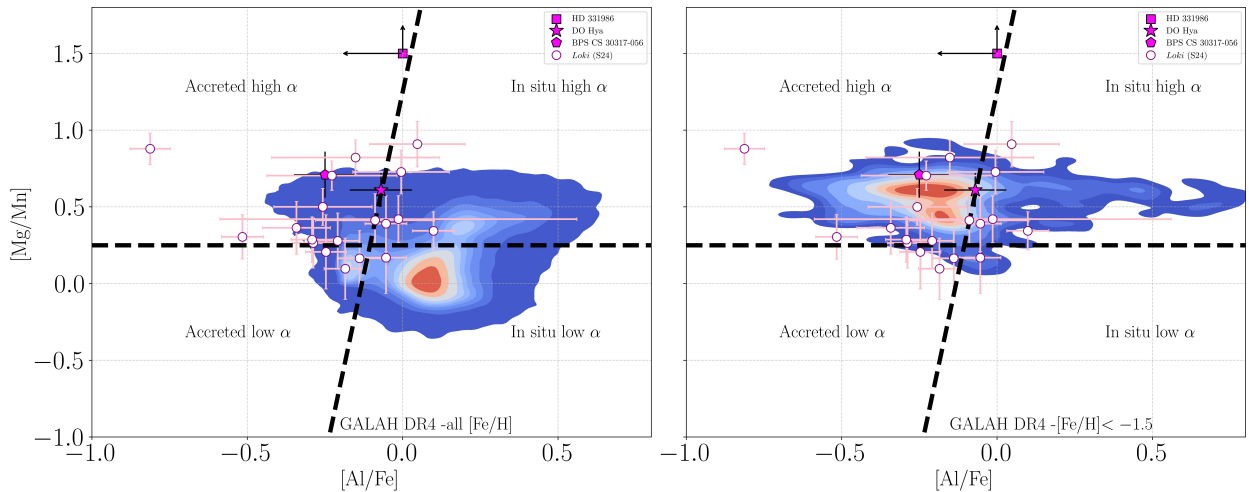


Fig. 2. [Mg/Mn] ratios as a function of [Al/Fe] for our three RRLs (filled markers) along with literature estimates, including GALAH DR4 (Buder et al. 2024, density plots in this figure) and *Loki* (empty circles) by Sestito et al. (2024).

3.2. Evolutionary timescales of EMP RR Lyrae stars

Our investigation reveals that, despite intrinsic differences in heavy element composition, EMPs are as common among RRLs as they are in the general field star population. Notably, evolutionary (Pietrinferni et al. 2021) and pulsation models (details are given in Appendix C) strongly support the existence of very metal-poor RRLs. The left panel of Fig. 4 illustrates a comparison between very metal-poor evolutionary models, which assume an α -enhanced chemical mixture with metal contents of $Z = 1 \times 10^{-5}$ and $Z = 2 \times 10^{-5}$, and the three EMP RRLs. To examine the positioning of the EMP RRLs, we plotted the zero-age horizontal branch (ZAHB, solid line) and the end of helium burning (dashed line). It is anticipated that low-mass, central helium-burning stars will spend the majority of their helium-burning phase between the ZAHB and the end-of-helium lines. Different symbols indicate the locations of two distinct stellar masses along the ZAHB and at the end of helium burning (as labelled). Furthermore, the blue and red vertical lines display the blue and red edges of the RRL instability strip (IS). Note that calculations provided by Marconi et al. (2015) did not include the very metal-poor regime ($Z \geq 10^{-4}$) and they were specifically computed for this investigation. Reddening, distances and mean magnitudes of the three EMP RRLs were adopted from different sources, depending on the star. For Figure 4 the optical mean magnitudes for HD 331986 are based on images collected with IAC80 telescope (see Appendix B), while NIR mean magnitudes are based on 2MASS measurements and light curve templates (Braga et al. 2019). The distance is based on Gaia DR3 parallax, according to Bailer-Jones et al. (2021). Moreover, we adopted a reddening estimate by Matsunaga (private communication) and the reddening law by Wang & Chen (2019).

For DO Hya and BPS CS 22881-039 the optical mean magnitudes come from ASAS-SN and Gaia $GB_p R_p$ transformed using Pancino et al. (2022), while NIR magnitudes from 2MASS. The distance was estimated using the PL in the WISE W1 pass-band Mullen et al. (2023), the reddening from Schlafly & Finkbeiner (2011) and the reddening law from Cardelli et al. (1989). The left panel of the same figure shows the comparison between theory and observations but in the optical-NIR $V-K$, K colour-magnitude diagrams (CMD). The $V-K$ is more sensitive to temperature variations and the K is one order of magnitude less affected by uncertainties in reddening correction.

The data presented in Fig. 4 demonstrate a remarkable agreement between theoretical predictions and observations. The three EMP RRLs appear to behave as canonical HB stars during their evolution off the ZAHB, with the ZAHBs in this extremely metal-poor range reaching effective temperatures that are generally hotter than the RRL IS (see Appendix C for further details). The main finding from comparing the evolutionary lifetimes of EMP and metal-poor stars within the instability strip is that the difference is only a factor of two to three. This suggests that we should be able to detect more EMP RRLs as larger catalogues (see e.g. Medina et al. 2024) and samples of spectra become available, such as those from upcoming large-scale surveys such as 4MOST (de Jong 2019) and WEAVE (Jin et al. 2024).

4. Concluding remarks

This study presents a detailed spectroscopic analysis of three EMP RRLs, pushing the boundaries of known metallicity for this old stellar tracer. Our high-resolution spectroscopic NLTE analysis yielded abundances for key elements (Fe, Al, Mg, Ca, Ti, Mn, and Sr). Kinematic analysis revealed a diverse origin for these stars: HD 331986 exhibits disc kinematics, while DO Hya and BPS CS 30317-056 are consistent with halo populations, highlighting the ubiquity of such very metal-deficient variable stars across the Galactic components.

Interestingly, the commonly used [Al/Fe] and [Mg/Mn] ratios, effective in distinguishing accreted and *in-situ* stellar populations at higher metallicities, proved less effective for $[Fe/H] \lesssim -1.5$. This challenges the current understanding of Galactic chemical evolution at the lowest metallicities and underscores the need for more sophisticated chemical tagging techniques. The observed [Sr/Fe] ratios display considerable variation amongst the three stars, suggesting a complex nucleosynthesis history and reinforcing the limitations of using single elemental ratios for tracing stellar origins. The results also highlight the need for further investigations into the production of r-process elements at extremely low metallicities.

Our theoretical models strongly support the existence of EMP RRLs; further observational studies are required to identify more EMP RRLs and refine our understanding of Galactic chemical evolution and stellar nucleosynthesis at extremely low metallicities.

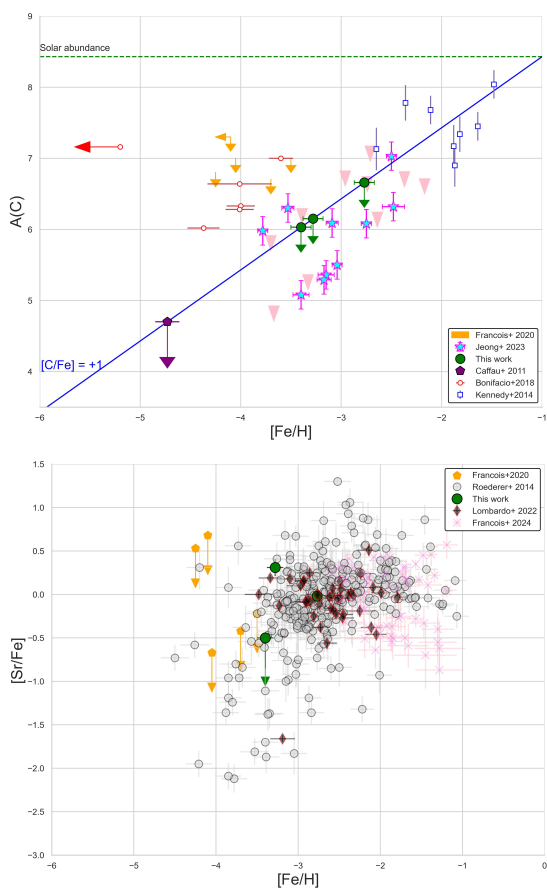


Fig. 3. Carbon and Sr as a function of $[Fe/H]$. Upper panel: C abundances for our three EMP RRLs (green points) as a function of $[Fe/H]$. For comparison, we include also stars from Jeong et al. (2023); François et al. (2020); Bonifacio et al. (2018); Caffau et al. (2011); Kennedy et al. (2014). All abundances are in LTE; the blue solid line marks $[C/Fe] = +1$, see e.g. Beers & Christlieb (2005). Lower panel: $[Sr/Fe]$ ratios vs. $[Fe/H]$ for our RRLs along with literature samples (Roederer et al. 2014; François et al. 2020, 2024; Lombardo et al. 2022). We provide NLTE abundances as done by François et al. (2024), while LTE values were given by Roederer et al. (2014); François et al. (2020); Lombardo et al. (2022).

Data availability

Appendices D-E are available on Zenodo (at this link)

Acknowledgements. This research was supported by the Munich Institute for Astro-, Particle and BioPhysics (MIAPbP) which is funded by the Deutsche Forschungsgemeinschaft (DFG, German Research Foundation) under Germany's Excellence Strategy – EXC-2094 – 390783311. M.M. and M.S.B. acknowledge support from the Agencia Estatal de Investigación del Ministerio de Ciencia e Innovación (MCIN/AEI) under the grant "RR Lyrae stars, a lighthouse to distant galaxies and early galaxy evolution" and the European Regional Development Fund (ERDF) with reference PID2021-127042OB-I00. This article is based on observations made with the IAC80 operated on the island of Tenerife by the Instituto de Astrofísica de Canarias in the Spanish Observatorio del Teide. SB acknowledges support from the Australian Research Council under grant number DE240100150. GI acknowledges support for this project from "La Caixa" Foundation (ID 100010434) under grant agreement "LCF/BQ/PI24/12040020". AB acknowledges support for this project from the European Union's Horizon 2020 research and innovation program under grant agreement No 865932-ERC-SNeX. C.E.M.-V. is supported by the international Gemini Observatory, a program of NSF NOIRLab, which is managed by the Association of Universities for Research in Astronomy (AURA) under a cooperative agreement with the U.S. National Science Foundation, on behalf of the Gemini partnership of Argentina, Brazil, Canada, Chile, the Republic of Korea, and the United States of America. Part of this work is based on archival data, software or online services provided by the Space Science Data Center - ASI. In particular, the GaiaPortal

access tool was used for this research (<http://gaiaportal.ssdsc.asi.it>). We would like to express our gratitude to the reviewer for their thorough examination of the manuscript and for their insightful comments and suggestions, which have enhanced the quality of our work.

References

- Akhlaghi, M. 2018, Gnuastro: GNU Astronomy Utilities, Astrophysics Source Code Library, record ascl:1801.009
- Andrae, R., Rix, H.-W., & Chandra, V. 2023, *ApJS*, 267, 8
- Arcones, A. & Thielemann, F.-K. 2023, *A&A Rev.*, 31, 1
- Arentsen, A., Placco, V. M., Lee, Y. S., et al. 2022, *MNRAS*, 515, 4082
- Baade, W. 1958, *Ricerche Astronomiche*, 5, 3
- Bailer-Jones, C. A. L., Rybizki, J., Fouvésneau, M., Demleitner, M., & Andrae, R. 2021, *AJ*, 161, 147
- Beers, T. C. & Christlieb, N. 2005, *ARA&A*, 43, 531
- Bellazzini, M., Massari, D., Ceccarelli, E., et al. 2024, *A&A*, 683, A136
- Bennett, M. & Bovy, J. 2019, *MNRAS*, 482, 1417
- Bergemann, M. 2011, *MNRAS*, 413, 2184
- Bergemann, M., Collet, R., Amarsi, A. M., et al. 2017, *ApJ*, 847, 15
- Bergemann, M., Gallagher, A. J., Eitner, P., et al. 2019, *A&A*, 631, A80
- Bergemann, M., Hansen, C. J., Bautista, M., & Ruchti, G. 2012a, *A&A*, 546, A90
- Bergemann, M., Lind, K., Collet, R., Magic, Z., & Asplund, M. 2012b, *MNRAS*, 427, 27
- Bertin, E. 2006, in *Astronomical Society of the Pacific Conference Series*, Vol. 351, *Astronomical Data Analysis Software and Systems XV*, ed. C. Gabriel, C. Arviset, D. Ponz, & S. Enrique, 112
- Bertin, E. & Arnouts, S. 1996a, *A&AS*, 117, 393
- Bertin, E. & Arnouts, S. 1996b, *A&AS*, 117, 393
- Bobrick, A., Iorio, G., Belokurov, V., et al. 2024, *MNRAS*, 527, 12196
- Bonifacio, P., Caffau, E., Spite, M., et al. 2018, *A&A*, 612, A65
- Bovy, J. 2015, *ApJS*, 216, 29
- Braga, V. F., Crestani, J., Fabrizio, M., et al. 2021, *ApJ*, 919, 85
- Braga, V. F., Stetson, P. B., Bono, G., et al. 2019, *A&A*, 625, A1
- Buder, S., Kos, J., Wang, E. X., et al. 2024, arXiv e-prints, submitted to PASA, arXiv:2409.19858
- Caffau, E., Bonifacio, P., François, P., et al. 2011, *Nature*, 477, 67
- Cardelli, J. A., Clayton, G. C., & Mathis, J. S. 1989, *ApJ*, 345, 245
- Chadid, M., Sneden, C., & Preston, G. W. 2017, *ApJ*, 835, 187
- Clementini, G., Ripepi, V., Garofalo, A., et al. 2023, *A&A*, 674, A18
- Cosentino, R., Lovis, C., Pepe, F., et al. 2014, in *Society of Photo-Optical Instrumentation Engineers (SPIE) Conference Series*, Vol. 9147, *Ground-based and Airborne Instrumentation for Astronomy V*, ed. S. K. Ramsay, I. S. McLean, & H. Takami, 91478C
- Cowan, J. J., Sneden, C., Lawler, J. E., et al. 2021, *Reviews of Modern Physics*, 93, 015002
- Crestani, J., Braga, V. F., Fabrizio, M., et al. 2021a, *ApJ*, 914, 10
- Crestani, J., Fabrizio, M., Braga, V. F., et al. 2021b, *ApJ*, 908, 20
- Das, P., Hawkins, K., & Jofré, P. 2020, *MNRAS*, 493, 5195
- de Jong, R. 2019, in *Preparing for 4MOST*, 1
- De Silva, G. M., Freeman, K. C., Bland-Hawthorn, J., et al. 2015, *MNRAS*, 449, 2604
- D'Orazi, V., Storm, N., Casey, A. R., et al. 2024, *MNRAS*, 531, 137
- Drimmel, R. & Poggio, E. 2018, *Research Notes of the American Astronomical Society*, 2, 210
- Ezzeddine, R., Merle, T., Plez, B., et al. 2018, *A&A*, 618, A141
- For, B.-Q., Sneden, C., & Preston, G. W. 2011, *ApJS*, 197, 29
- François, P., Cescutti, G., Bonifacio, P., et al. 2024, *A&A*, 686, A295
- François, P., Wanajo, S., Caffau, E., et al. 2020, *A&A*, 642, A25
- Gerber, J. M., Magg, E., Plez, B., et al. 2023, *A&A*, 669, A43
- GRAVITY Collaboration, Abuter, R., Amorim, A., et al. 2018, *A&A*, 615, L15
- Hansen, C. J., Nordström, B., Bonifacio, P., et al. 2011, *A&A*, 527, A65
- Hauck, B. & Mermilliod, M. 1998, *A&AS*, 129, 431
- Hawkins, K., Jofré, P., Masseron, T., & Gilmore, G. 2015, *MNRAS*, 453, 758
- Hidalgo, S. L., Pietrinferni, A., Cassisi, S., et al. 2018, *ApJ*, 856, 125
- Horta, D., Schiavon, R. P., Mackereth, J. T., et al. 2021, *MNRAS*, 500, 1385
- Horta, D., Schiavon, R. P., Mackereth, J. T., et al. 2023, *MNRAS*, 520, 5671
- Inno, L., Matsunaga, N., Romaniello, M., et al. 2015, *A&A*, 576, A30
- Jeong, M., Lee, Y. S., Beers, T. C., et al. 2023, *ApJ*, 948, 38
- Jin, S., Trager, S. C., Dalton, G. B., et al. 2024, *MNRAS*, 530, 2688
- Karakas, A. I. & Lattanzio, J. C. 2014, *PASA*, 31, e030
- Kennedy, C. R., Stancliffe, R. J., Kuehn, C., et al. 2014, *ApJ*, 787, 6
- Lang, D., Hogg, D. W., Mierle, K., Blanton, M., & Roweis, S. 2010, *AJ*, 139, 1782
- Layden, A. C. 1995, *AJ*, 110, 2312
- Layden, A. C., Hanson, R. B., Hawley, S. L., Klemola, A. R., & Hanley, C. J. 1996, *AJ*, 112, 2110

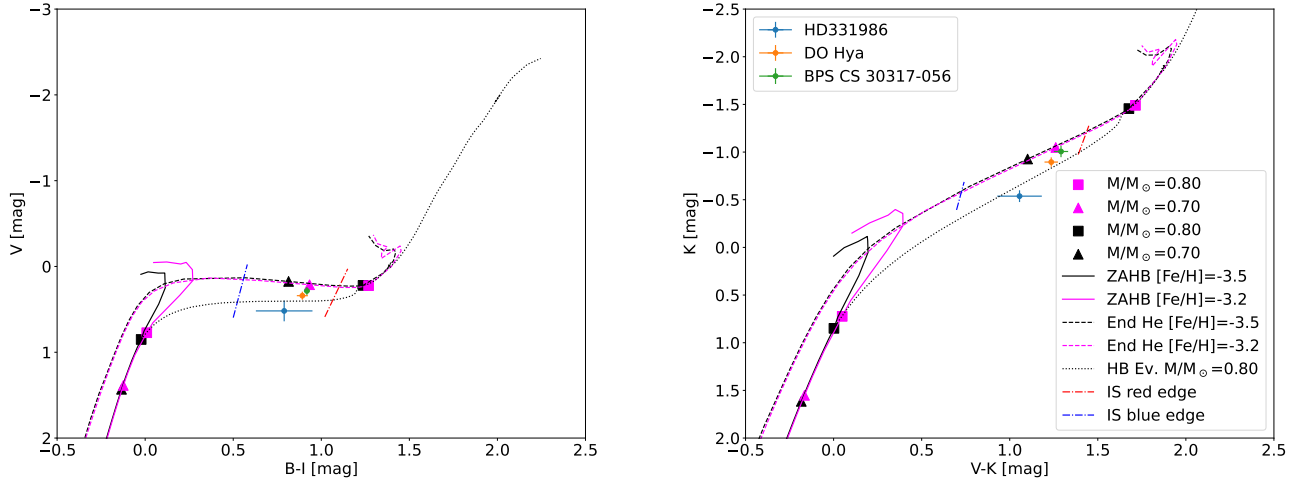


Fig. 4. Left – Optical $B-I$, V CMD showing the location of very metal-poor RRLs. The solid lines display predicted ZAHBs at different chemical compositions (see labelled values), while the dashed lines the central helium exhaustion for the same chemical compositions (Pietrinferni et al. 2021). Squares and triangles mark different stellar masses along the ZAHB and end-of-helium. The almost vertical lines display the blue (hot) and the red (cool) edge of the predicted RRL instability strip for $Z=1\times 10^{-5}$ specifically computed for this investigation (see text for more details). Right – Same as the left, but for the optical-NIR ($V-K$, K) CMD.

Lombardo, L., Bonifacio, P., François, P., et al. 2022, *A&A*, 665, A10
Magurno, D., Sneden, C., Bono, G., et al. 2019, *ApJ*, 881, 104
Magurno, D., Sneden, C., Braga, V. F., et al. 2018, *ApJ*, 864, 57
Marconi, M., Coppola, G., Bono, G., et al. 2015, *ApJ*, 808, 50
Marsakov, V. A., Gozha, M. L., & Koval', V. V. 2019, *Astronomy Reports*, 63, 203
Mashonkina, L., Jablonka, P., Sitnova, T., Pakhomov, Y., & North, P. 2017, *A&A*, 608, A89
Mashonkina, L., Korn, A. J., & Przybilla, N. 2007, *A&A*, 461, 261
Massari, D., Koppelman, H. H., & Helmi, A. 2019, *A&A*, 630, L4
Matsunaga, N., Itane, A., Hattori, K., et al. 2022, *ApJ*, 925, 10
Matsunaga, N., Jian, M., Taniguchi, D., & Elgueta, S. S. 2021, *MNRAS*, 506, 1031
McMillan, P. J. 2017, *MNRAS*, 465, 76
Medina, G. E., Muñoz, R. R., Carlin, J. L., et al. 2024, *MNRAS*, 531, 4762
Mullen, J. P., Marengo, M., Martínez-Vázquez, C. E., et al. 2022, *ApJ*, 931, 131
Mullen, J. P., Marengo, M., Martínez-Vázquez, C. E., et al. 2023, *ApJ*, 945, 83
Nepal, S., Chiappini, C., Queiroz, A. B., et al. 2024, *A&A*, 688, A167
Pancino, E., Marrese, P. M., Marinoni, S., et al. 2022, *A&A*, 664, A109
Pietrinferni, A., Hidalgo, S., Cassisi, S., et al. 2021, *ApJ*, 908, 102
Placco, V. M., Frebel, A., Beers, T. C., & Stancliffe, R. J. 2014, *ApJ*, 797, 21
Preston, G. W. 1959, *ApJ*, 130, 507
Preston, G. W. 1964, *ARA&A*, 2, 23
Preston, G. W., Sneden, C., Chadid, M., Thompson, I. B., & Shectman, S. A. 2019, *AJ*, 157, 153
Re Fiorentin, P., Spagna, A., Lattanzi, M. G., Cignoni, M., & Vitali, S. 2024, *ApJ*, 977, 278
Roederer, I. U., Preston, G. W., Thompson, I. B., et al. 2014, *AJ*, 147, 136
Schlafly, E. F. & Finkbeiner, D. P. 2011, *ApJ*, 737, 103
Semenova, E., Bergemann, M., Deal, M., et al. 2020, *A&A*, 643, A164
Sestito, F., Fernandez-Alvar, E., Brooks, R., et al. 2024, arXiv e-prints, submitted to *A&A*, arXiv:2409.13813
Sitnova, T. M., Mashonkina, L. I., Ezzeddine, R., & Frebel, A. 2019, *MNRAS*, 485, 3527
Skrutskie, M. F., Cutri, R. M., Stiening, R., et al. 2006, *AJ*, 131, 1163
Sneden, C., Preston, G. W., Chadid, M., & Adamów, M. 2017, *ApJ*, 848, 68
Spite, M., Andrievsky, S. M., Spite, F., et al. 2012, *A&A*, 541, A143
Stetson, P. B. 2000, *PASP*, 112, 925
Storm, N. & Bergemann, M. 2023, *MNRAS*, 525, 3718
Strassmeier, K. G., Ilyin, I., Järvinen, A., et al. 2015, *Astronomische Nachrichten*, 336, 324
Walker, A. R. & Terndrup, D. M. 1991, *ApJ*, 378, 119
Wallerstein, G., Gomez, T., & Huang, W. 2011, in *RR Lyrae Stars, Metal-Poor Stars, and the Galaxy*, ed. A. McWilliam, Vol. 5, 210
Wang, S. & Chen, X. 2019, *ApJ*, 877, 116
Zhang, H., Ardern-Arentsen, A., & Belokurov, V. 2024, *MNRAS*, 533, 889

Appendix A: Atmospheric parameters and abundances for our three EMP stars

In Table A.1 we provide atmospheric parameters and elemental abundances for the stars HD 331986, DO Hya, and BPS CS 30317-056. It includes T_{eff} , $\log g$, and V_{mic} , along with $[\text{Fe}/\text{H}]$, $[\text{Al}/\text{Fe}]$, $[\text{Mg}/\text{Fe}]$, $[\text{Ca}/\text{Fe}]$, $[\text{Ti}/\text{Fe}]$, $[\text{Mn}/\text{Fe}]$, and $[\text{Sr}/\text{Fe}]$, all derived in NLTE. Additionally, the table contains data on RV, pulsation periods, and classification types of each star, indicating their variability class with HD 331986 categorised as type RRc, while DO Hya and BPS CS 30317-056 are classified as RRab.

Table A.1. Atmospheric parameters, abundances, radial velocity, pulsation period and class of HD 331986, DO Hya and BPS CS 30317-056. All abundances are in NLTE with model atoms retrieved from the following sources: iron (Bergemann et al. 2012b; Semanova et al. 2020), calcium (Mashonkina et al. 2017; Semanova et al. 2020), titanium (Bergemann 2011), manganese (Bergemann et al. 2019), aluminium (Ezzeddine et al. 2018), magnesium (Bergemann et al. 2017), and strontium come from (Bergemann et al. 2012a; Gerber et al. 2023). The line list is available upon request.

star	T_{eff} (K)	$\log g$ (dex)	V_{mic} (km s^{-1})	$[\text{Fe}/\text{H}]$	$[\text{Al}/\text{Fe}]$	$[\text{Mg}/\text{Fe}]$	$[\text{Ca}/\text{Fe}]$	$[\text{Ti}/\text{Fe}]$	$[\text{Mn}/\text{Fe}]$	$[\text{Sr}/\text{Fe}]$	RV (km s^{-1})	Period (days)	class
HD331986	6450±80	2.90±0.10	3.5±0.5	-3.40 ± 0.05	< 0	0.50±0.05	0.21±0.10	---	< -1.00	< -0.5	-97.2±2.9	0.3711815	RRc
DO Hya	5835±80	2.50±0.10	3.1±0.5	-3.28 ± 0.02	-0.07 ± 0.10	0.55±0.03	0.22±0.10	0.61±0.02	-0.06±0.10	0.31±0.10	272.5±6.8	0.7133254	RRab
BPS CS 30317-056	6025±80	2.50±0.15	3.0±0.5	-2.77±0.05	-0.25±0.10	0.34±0.05	0.24±0.10	0.56±0.05	-0.37 ± 0.12	-0.02±0.08	-58.9±4.6	0.7484904	RRab

Appendix B: Photometric properties

We performed optical photometry for HD 331986 using the IAC80 telescope located at the Teide Observatory in Tenerife (Spain). We used two different photometric systems (i.e. wide-band Johnson-Cousins UBVRI and mid-band Strömgren uvby) to constrain the phase of the spectroscopic observations and determine a first estimate of different stellar parameters from the pulsation properties. We obtained a total of 600 epochs for UBVRI and 100 epochs for Strömgren, observing mainly during the summer of 2021. We carried out data reduction, aperture photometry and calibration of the scientific frames using a Python custom-based pipeline, `astrometry.net` (Lang et al. 2010), `SCAMP` (Bertin 2006), `SExtractor` (Bertin & Arnouts 1996a), and `gnuastro` (Akhlaghi 2018). We standardised the photometry using the same pipeline, aligning it with the Landolt system for the Johnson-Cousins filters (Stetson 2000) and the Hauck & Mermilliod system for the Strömgren filters (Hauck & Mermilliod 1998). The precision achieved in the photometry was between 0.01 and 0.03 magnitudes for the UBVRI passbands and between 0.02 and 0.10 magnitudes for the Strömgren passbands. This precision decreases toward the bluer filters due to the lower quantum efficiency of the CCD. The resulting light curve is presented in Figure B.1.

We acquired near-infrared photometry for HD331986 using the Nishiharima Infrared Camera (NIC) on the 2.0 m Nayuta telescope at the Nishi-Harima Astronomical Observatory. The observations were made at 14 epochs in 2021 November. Reduction of the images followed a standard procedure for near-infrared images, including dark subtraction and flat-field correction. The aperture photometry was made also with `SExtractor` (Bertin & Arnouts 1996b) and the photometric zero points was determined by comparing the measurements of ~ 20 stars in the $2'.73 \times 2'.73$ field-of-view with their JHKs magnitudes in the 2MASS catalogue (Skrutskie et al. 2006). Figure B.2 shows the light curves. The mean magnitudes were obtained with fitting light-curve templates (Braga et al. 2019).

For the reddening estimate, we used an extinction of $A_V=0.85$ mag, derived by Matsunaga et al. (2021). We adopted the reddening law from Schlafly & Finkbeiner (2011), obtaining the following corrections for each of the Strömgren passbands:

$$c_u = 1.61$$

$$c_b = 1.25$$

$$c_v = 1.41$$

$$c_y = 1.00$$

Strömgren photometry can be used to define several colour indices that are sensitive to different stellar parameters, that is, temperature, surface gravity, and metallicity. These indices are defined as follow:

(b-y), for temperature

$$c_1 = (u-v)-(v-b), \text{ for surface gravity}$$

$$m_1 = (v-b)-(b-y), \text{ for metallicity}$$

As so, we computed both c_1 index and the reddening-free $[c_1]$ (defined as $[c_1] = c_1 - 0.19 (b-y)$) for every epoch, before and after applying the reddening correction, obtaining the following mean values:

$$c_1 = 1.28 \pm 0.28$$

$$c_1 \text{ with de-reddened magnitudes } c_1 = 1.25 \pm 0.28$$

$$[c_1] = 1.20 \pm 0.28$$

$$[c_1] \text{ with de-reddened magnitudes } [c_1] = 1.22 \pm 0.28$$

To study the relation among c_1 index and surface gravity, we employed a set of synthetic CM diagrams covering a broad range in metallicities ($[Fe/H] = -0.09, -3.62$), obtained using the BaSTI horizontal branch evolutionary models (Hidalgo et al. 2018). The synthetic HB models were adopted to investigate on a quantitative basis the possible dependence of the c_1 - $\log g$ relation on the metal content for effective temperatures and surface gravities typical of RRLs. Figure B.3 shows the synthetic HB models for twelve different iron abundances and the red dots mark the predicted RRLs adopted to derive the c_1 - $\log g$ relation. We performed a linear fit over the entire data set, namely selecting stars located inside the RRL instability strip, i.e. objects with an effective temperature ranging from ~ 5600 K to ~ 8000 K. Interestingly enough, we found no significant dependence on the iron abundance, as can be seen on the left panel of Figure B.4. This shows the linear fit for each metallicity diagram together with a plot with the dependency of the slope and intercept with the metallicity. Taking this into account, we joined together all the CMDs to obtain a single and simpler relation between the surface gravity and the $c_1/[c_1]$ indices, the second one being a reddening free index, as noted previously in the text. This is valid in the selected range of temperatures and has a linear dependency as follows:

$$\log g \text{ (cgs)} = m c_1 + n$$

$$m = 0.763 \pm 0.003$$

$$n = 2.131 \pm 0.002$$

$$\log g \text{ (cgs)} = m [c_1] + n$$

$$m = 0.713 \pm 0.002$$

$$n = 2.208 \pm 0.002$$

As a final step, surface gravity was computed from this relation and the $c_1/[c_1]$ index that arose from photometry at the same phase where the spectra were gathered. There is excellent agreement between our photometric and spectroscopic surface gravity $\log g$ (difference less than 0.1 dex).

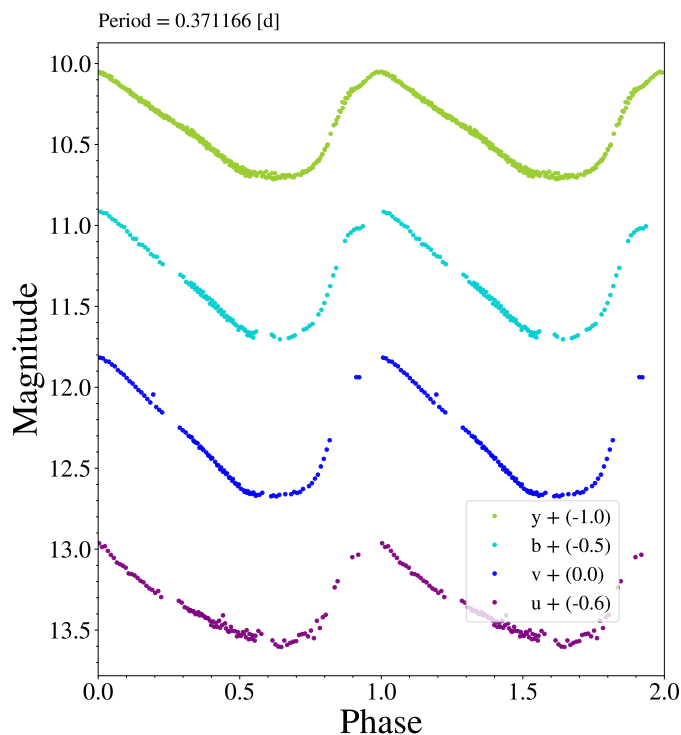


Fig. B.1. Light curves of HD 331986 in Strömgren *ybv* filters. Magnitudes other than *b* are artificially shifted by the number indicated in the legend for the sake of a better representation in a single plot.

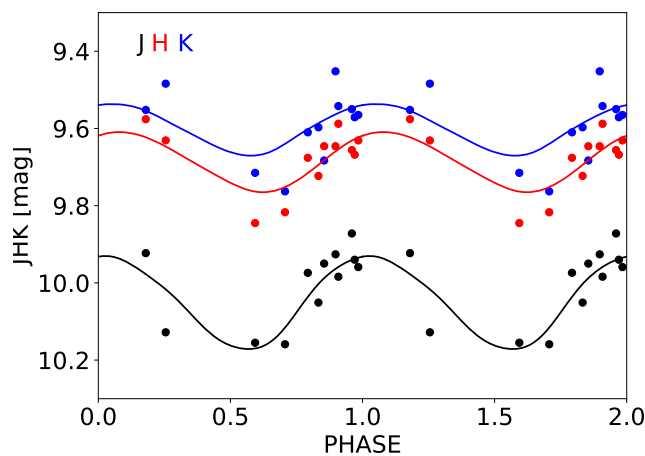


Fig. B.2. Black, red and blue circles represent the *J*-, *H*- and *K*- band data for HD 331986 collected with NIC at Nayuta Telescope in November 2021. Solid lines of the same colour represent the light curve templates by Braga et al. (2019), adopted to fit the empirical data.

Appendix C: Theoretical models

To provide a more comprehensive theoretical framework for low-mass central helium-burning stars, Figure C.1 shows in the Hertzsprung-Russell diagram predicted ZAHBs (black dashed lines), end-of-central-helium burning (purple dashed lines) and representative HB evolutionary models (solid lines) for a wide range of metal-poor and extremely metal-poor α -enhanced chemical compositions (see labelled values). Note that the current ZAHBs have been constructed by assuming a progenitor age of 13.5 Gyr at the tip of the red giant branch. The location on the ZAHB and on the end-of-helium burning of this progenitor mass are marked with filled circles.

The predicted instability strip for RRLs provided by Marconi et al. (2015) only covers the metal-poor regime ($[\text{Fe}/\text{H}] \sim -2.50$, $Z=1 \times 10^{-4}$). Therefore, we performed detailed calculations, using non-linear pulsation models, including a time-dependent treatment of the convective transport, for an α -enhanced chemical composition of $[\text{Fe}/\text{H}] \sim -3.62$ ($Z=1 \times 10^{-5}$). The new instability strip is plotted in the top left panel of Fig. C.1 and the edges are listed in Table C.1, alongside their optical and NIR magnitudes. The instability strip for $[\text{Fe}/\text{H}] \sim -3.20$ ($Z=2 \times 10^{-5}$) was linearly interpolated.

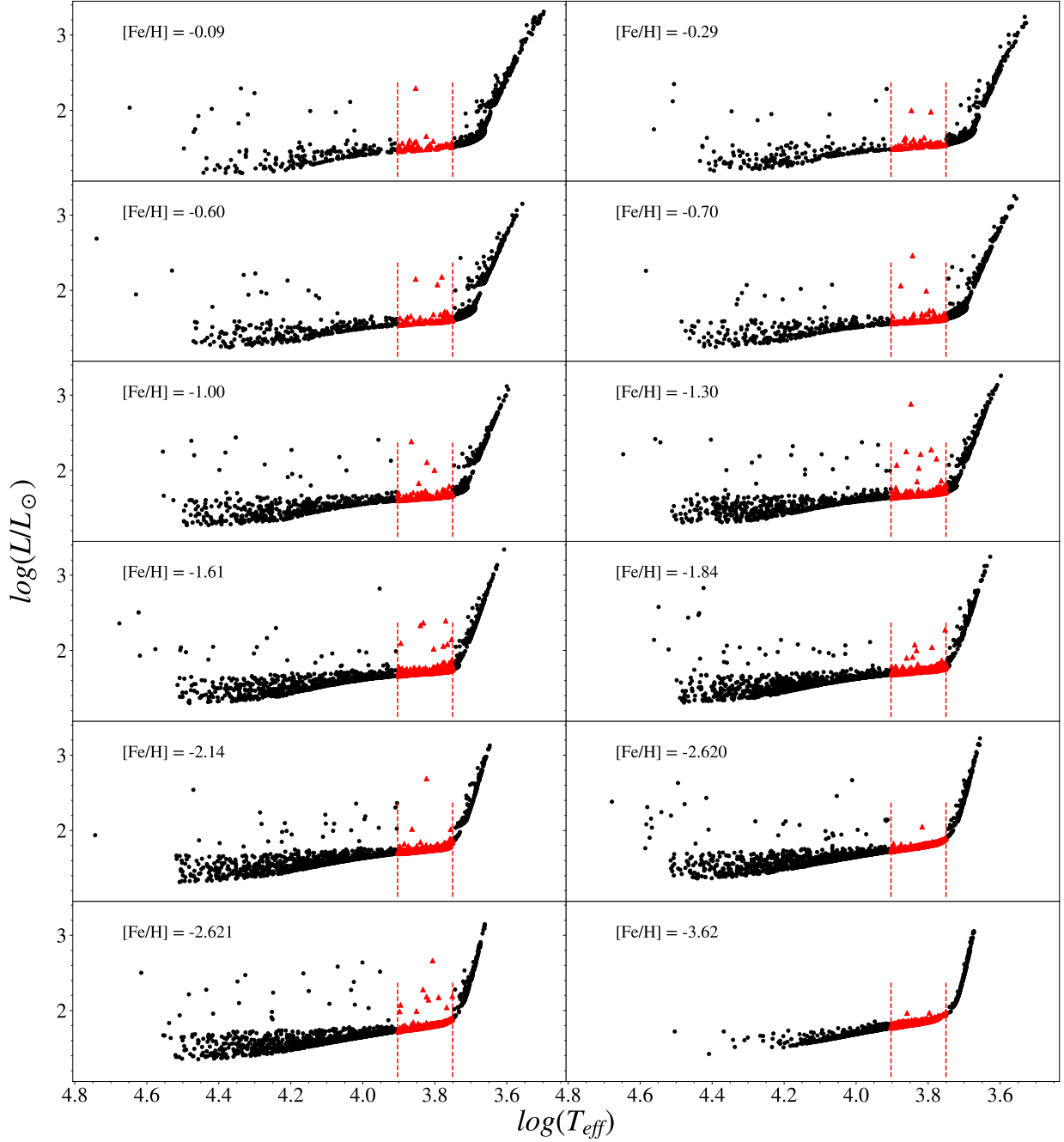


Fig. B.3. Hertzsprung Russell diagrams for the simulated HBs. Each panel shows a synthetic HB for different metal abundances (see labeled values). The dashed vertical lines display the blue (hot) and the red (cool) edge of the RRL instability strip.

Table C.1. Edges of the instability strip.

Edge	M/Mo	logL/Lo	Te	M_V	$B - V$	$U - B$	$V - I$	$V - R$	$R - I$	$V - J$	$V - K$
FOBE	0.85	1.78	7250	0.305	0.20292	0.055	0.318	0.140	0.177	0.530	0.698
FBE	0.85	1.78	7050	0.317	0.23346	0.030	0.367	0.164	0.202	0.604	0.802
FORE	0.85	1.78	6450	0.369	0.33261	-0.045	0.519	0.238	0.280	0.846	1.140
FRE	0.85	1.78	6050	0.415	0.41022	-0.081	0.624	0.290	0.333	1.021	1.389
FOBE	0.85	1.88	7150	0.054	0.21277	0.054	0.337	0.149	0.187	0.561	0.741
FBE	0.85	1.88	6950	0.067	0.24373	0.029	0.387	0.173	0.213	0.637	0.847
FORE	0.85	1.88	6550	0.103	0.31103	-0.021	0.489	0.223	0.265	0.799	1.074
FRE	0.85	1.88	5950	0.173	0.42928	-0.075	0.649	0.303	0.345	1.063	1.449

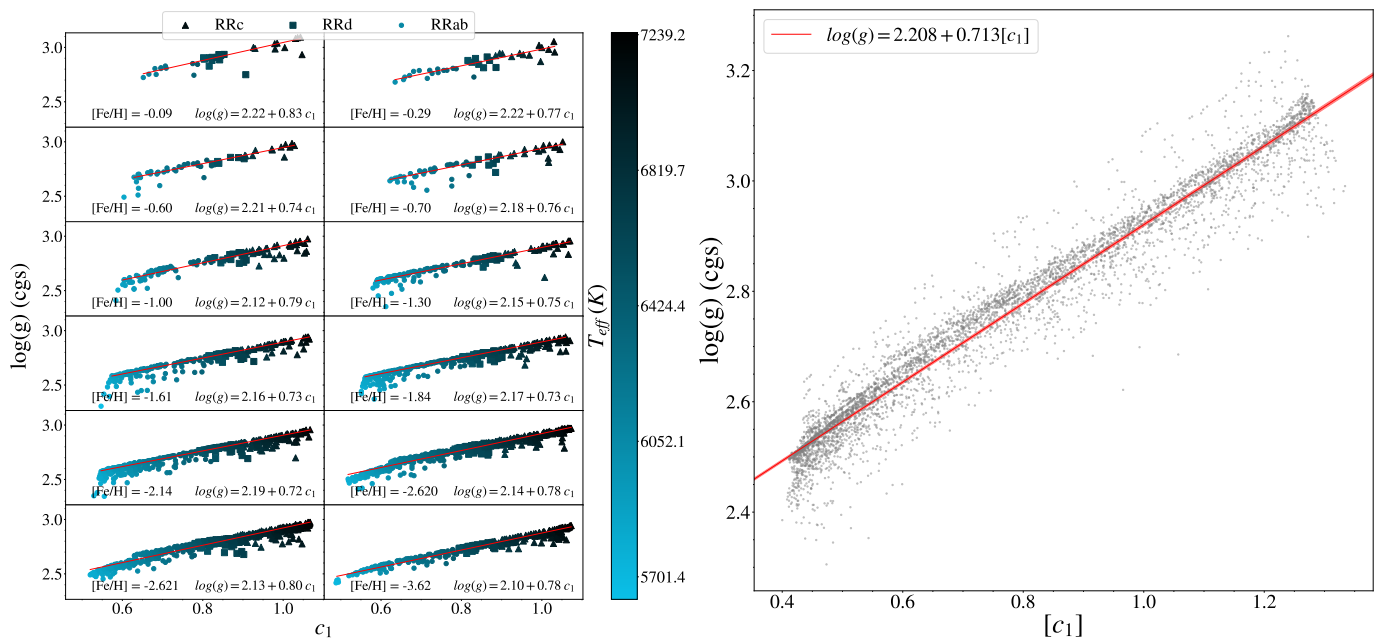


Fig. B.4. Left - c_1 coefficient as a function of surface gravity measured in cgs units. Each of the frames represents this relation for a different $[\text{Fe}/\text{H}]$ in the range $(-0.09, -3.62)$. Both the metallicity and the parameters of the fit are over-impressed in the bottom central area of each frame. Points are colour-coded according to the effective temperature of each star. Right - $[c_1]$ coefficient as a function of surface gravity. In this plot, all the metallicities have been joined together to compute a relation for the whole set of parameters at once, given that dependency with $[\text{Fe}/\text{H}]$ is negligible, as seen in the left panel.

Table C.2. Evolutionary time spent inside the instability strip for different chemical compositions.

M	Y	Z	$[\text{Fe}/\text{H}]$	$t(\text{IS}_{end})$	$t(\text{IS}_{start})$	(IS_{cross})
M_{\odot}				Myr	Myr	Myr
0.68	0.24	0.00001	-3.62	77.5	69.2	8.3
0.85	0.24	0.00001	-3.62	62.6	44.5	18.0
0.68	0.24	0.00002	-3.20	78.6	68.7	9.9
0.80	0.24	0.00002	-3.20	65.9	47.8	18.1
0.66	0.24	0.0001	-2.50	84.6	78.2	6.4
0.80	0.24	0.0001	-2.50	67.9	43.3	24.7
0.65	0.25	0.0002	-2.20	87.2	78.3	8.9
0.80	0.25	0.0002	-2.20	61.9	1.0	60.9
0.63	0.25	0.0004	-1.90	92.5	87.5	5.0
0.72	0.25	0.0004	-1.90	70.4	1.0	69.4
0.62	0.25	0.0006	-1.71	93.4	82.7	10.7
0.70	0.25	0.0006	-1.71	63.7	1.0	62.7

The current evolutionary and pulsation prescriptions indicate that for iron abundances more metal-poor $[\text{Fe}/\text{H}] \sim -2.20$ ($Z=2 \times 10^{-4}$), the ZAHBs (black dashed lines) based on old progenitors either do not cross or minimally cross the instability strip, that is the ZAHB attains colours that are systematically bluer (hotter) than the predicted RRL instability strip. The consequence is that in the very metal-poor and metal-poor regime ($[\text{Fe}/\text{H}] \leq -2.2$) RRLs can only be produced by stars during their off-ZAHB evolution.

The consequence of the systematic shift toward higher effective temperatures in the extremely metal-poor regime is that these stars are expected to spend, on average, two to three times less time inside the IS compared to their metal-poor and metal-intermediate counterparts. Evolutionary prescriptions listed in Table C.2 indicate that given an increase in iron abundance of ~ 1.5 dex, from $[\text{Fe}/\text{H}] = -3.6$ to $[\text{Fe}/\text{H}] = -2.2$, the evolutionary time spent inside the IS ranges from ~ 25 – 30 Myr in the very metal-poor regime to ~ 70 Myr in more metal-rich stars. Note that in these preliminary estimates we are assuming that the mass distribution inside the IS is linear over the entire range in effective temperatures covered by the IS. Moreover, we are also assuming that the star formation rate in moving from the very metal-poor stars to the more metal-rich ones is constant in time. Despite these assumptions, the statistics of EMP RRLs, which occur at a rate well below the 1%, align with the occurrence rate of stars with metallicity $[\text{Fe}/\text{H}] \lesssim -2.75$ (see e.g. Andrae et al. (2023)) and there is no significant tension as we observe consistent numbers.

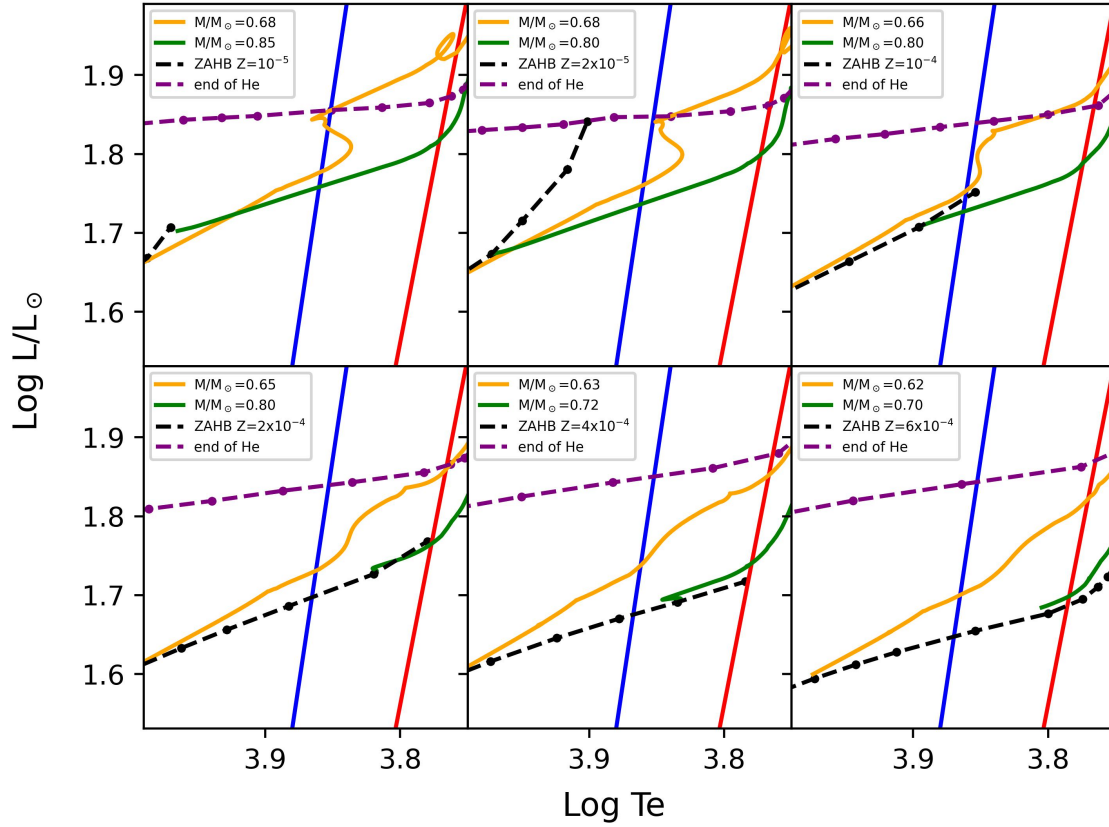


Fig. C.1. Hertzsprung-Russell diagram for low-mass stars during central helium-burning phases. The different panels display predictions for different metal-poor and extremely metal-poor chemical compositions (see labelled values). The dashed lines show the ZAHB (black) and the end-of-central-helium burning (endHB, purple). Coloured lines are selected HB evolutionary models showing the typical RRL crossing of the IS. The green line shows the evolutionary path of a star close to the ZAHB while the orange line the evolutionary path of a low-mass evolved RRL. Masses that produced RRLs are highlighted in the legend. The almost vertical blue and red lines display the predicted RRL instability strip from Marconi et al. (2015) updated with extremely metal-poor pulsation models at $Z=0.00001$.